ACS APPLIED MATERIALS & INTERFACES

www.acsami.org

Research Article

Pressure- and Temperature-Induced Structural Phase Diagram of Lead-Free $(K_{0.5}Na_{0.5})NbO_3-0.05LiNbO_3$ Single Crystals: Raman Scattering and Infrared Study

Yuting Yan, Anyang Cui, Kai Dai, Yan Ye, Kai Jiang,* Jinzhong Zhang, Jiajia Feng, Hongliang Dong, and Zhigao Hu*

Cite This: *ACS Appl. Mater. Interfaces* 2022, 14, 45590−45599

Read Online

ACCESS | Metrics & More | Article Recommendations

ABSTRACT: Ferroelectric lead-free $K_xNa_{1-x}NbO_3$ (KNN) perovskite, whose piezoelectric properties can be comparable to those of traditional Pb-based systems, has aroused wide concern in recent years. However, the specific influences of the stress field on KNN's structure and piezoelectric properties have not been well clarified and there are few descriptions about the temperature−pressure phase diagram. Here, we analyzed the phonon mode behavior and structural evolution of $K_{0.5}Na_{0.5}NbO_3$-0.05$LiNbO_3$ (KNN-LN) and MnO_2-doped single crystals with pressure- and temperature-dependent phase structure variations by theoretical calculation, polarized Raman scattering, and infrared reflectance spectra. The different phase structures can be predicted at high pressure using the CALYPSO method with its same-name code. The rhombohedral → orthorhombic → tetragonal → cubic phase transition process can be discovered in detail by Raman spectra under different temperatures and pressures. The phase coexistence on the thermal phase boundary was confirmed by basic anastomosis. Meanwhile, it was found that the substitution of Mn in the NbO_6 octahedron aggravates the deformation of high pressure on KNN-LN and the substitution of Mn at the B-site intensifies the structural evolution more severely than at the A-site. The present study aims at exploring octahedra tilt, phonon vibrations, and the internal structure on the general critical phase boundary in KNN-LN crystals. It provides effective help for the study of lead-free perovskite phase transformation and the improvement in piezoelectric properties under a high-pressure field.

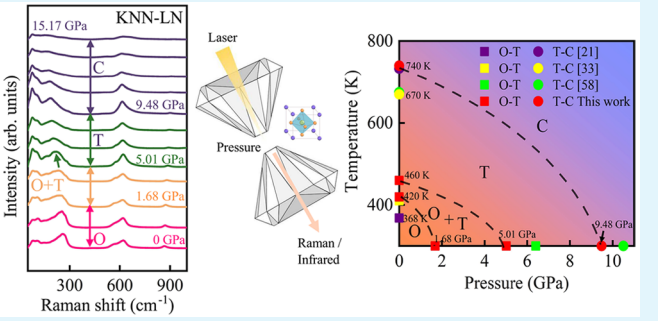

KEYWORDS: *potassium sodium niobate, phase boundary, multiphase coexistence, Raman spectroscopy, high pressure, phase diagram*

INTRODUCTION

Potassium sodium niobate $(K_xNa_{1-x})NbO_3$ (KNN) and its derivatives have been considered as an environmentally friendly alternative for $Pb(Zr_xTi_{1-x})O_3$ (PZT) owing to their excellent piezoelectric properties.[1−6] Over the past few years, in order to eliminate the pollution caused by the manufacturing process of lead-based materials, the urgent need for the application of lead-free materials based on KNN in sensors, resonators, and other electromechanical fields[7−9] has played an increasingly essential role.[10−12] Therefore, KNN-based single crystals will probably benefit from attracting more attention, as they show a high piezoelectric coefficient (d_{33}) of approximately 205−405 pC/N with a high Curie temperature of 697 K.[13−15] With the development of technology in the field, how to enhance the piezoelectric properties of KNN by improving the doping and synthesis methods has become a hot issue. However, significant enhancement of piezoelectricity is usually observed near the phase boundary, wherein the crystal structure changes abruptly. As shown in Figure 1a, the majority of the studies on KNN are related to phase boundaries. High piezoelectricity (d_{33} > 600 pC/N) was found in KNN with phase boundary by Li et al.[16] Due to the enhanced polarizability, the anomalously high dielectric and piezoelectric properties near the morphotropic phase boundary (MPB)[11,17−20] among rhombohedral (R), tetragonal (T), and orthorhombic (O) phases make it important to confirm the phase boundary.[21] The MPB contains multiphase coexistence and is influenced by composition below the Curie temperature (T_C). It is necessary to find the relationships between the lattice symmetry, structure evolution, and KNN-based ferroelectric performances with MPB composition, which can

Received: July 30, 2022
Accepted: September 22, 2022
Published: October 3, 2022

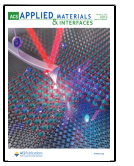

https://doi.org/10.1021/acsami.2c13669
ACS Appl. Mater. Interfaces 2022, 14, 45590−45599

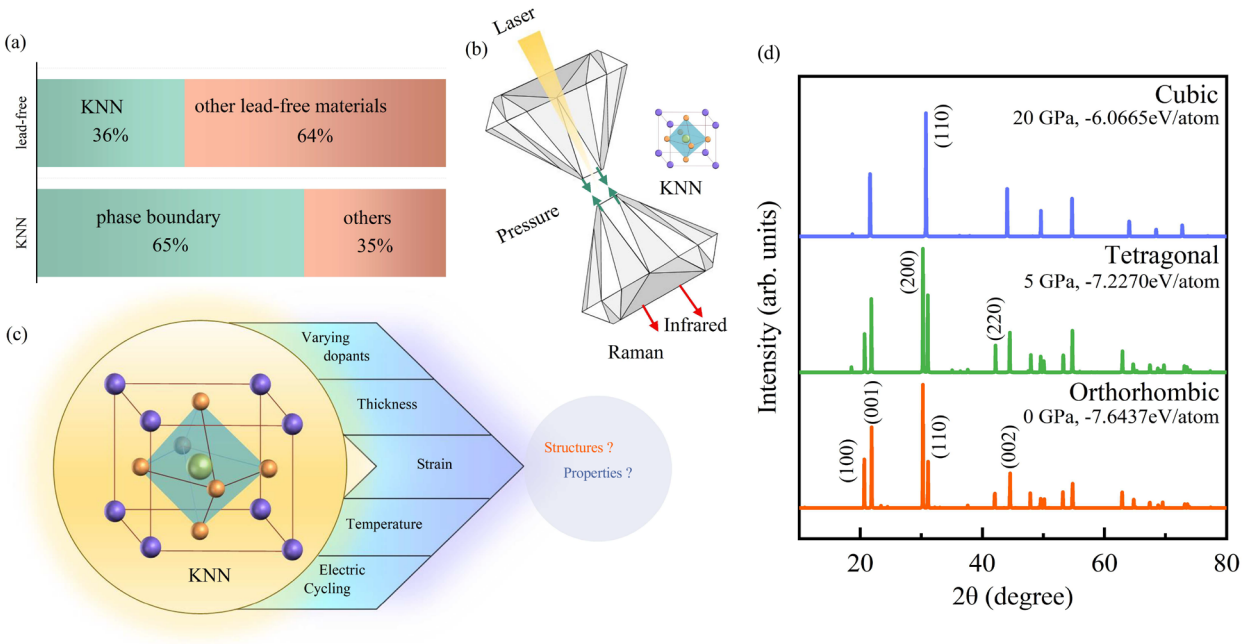

Figure 1. (a) Current investigations of lead-free materials and KNN-based studies. The KNN data were collected from the ISI Web of Science using the keywords "KNN", "piezoelectric", and "lead-free", while the phase boundary data were collected using the keywords "phase boundary", "KNN", "piezoelectric", and "lead-free". (b) Structure diagram of a diamond anvil cell (DAC) in pressure-dependent studies. (c) Structure and property evolutions under possible external field regulations. (d) XRD pattern and static energy of KNN-LN material with different structural phases (orthogonal, tetragonal, and cubic) based on the theoretical calculations. Note that some main diffraction peaks have been assigned to the corresponding crystal plane.

enrich the recognition of structure-dependent piezoelectric contribution. Since the first exploration of the phase boundary of KNN-based ceramics in 2004,[1] excellent piezoelectric properties have been continuously obtained in KNN with an O-T phase boundary. Various studies on the O-T phase boundary have accumulated rich experience on how to select effective potential additives for KNN.[22−24] In general, the phase boundary in KNN crystals can be regarded as the intrinsic features of polymorphic phase transition (PPT), which can shift to room temperature by adjusting element doping.[25,26] Li^+ substitution has been studied in depth to construct the O-T phase boundary.[27,28] Moreover, as a comprehensive and useful additive, the Mn ions in MnO_2 have different valence states (+2, +3, and +4).[7,12] On the other hand, the single crystal has leakage current on account of the presence of lattice defects.[13,22] Low leakage current and the additional high antifatigue properties in Mn-doped KNN crystals were obtained in recent work.[29] In the condition of KNN-LN doped with MnO_2, Mn ions substitute A or B sites as electron or hole absorber during oxidation.[30] The Mn ion can absorb the surplus positive charge, which could effectively reduce leakage current.[31−35] A high d_{33} of 1050 pC/N with O-T was obtained in KNN-$LiBiO_3$-MnO_2 single crystals by using the seed-free solid-state crystal growth (SFSSCG) method.[32] However, the internal physical correlations between Mn-doping and phase transition points are still worth exploring. The specific phase transition properties and lattice structure evolution of KNN remain to be studied to achieve more excellent piezoelectric properties.

In recent years, research studies on temperature-dependent engineering of KNN-based materials have been reported frequently. The specific structure and properties evolutions of KNN under field regulations have attracted much attention, as plotted in Figure 1c. As one of the external field regulation methods, the stress field is gradually regarded as an effective method to investigate the possible changes in structures and properties near the phase boundary. It would allow for variation in interatomic distances and chemical bonds[36] so that whether pressure can optimize piezoelectric properties near the O-T phase boundary to a greater extent than other external factors such as temperature is worth discussing. Low-symmetry perovskite under ambient conditions at room temperature and pressure usually transforms to highly symmetrical structures with smaller inclination as the pressure increases.[37] The relative compressibility of AX_{12} and BX_6 sites causes the perovskite structure to become more distorted as the pressure increases. The BO_6 octahedron tilts with increasing pressure, which can be reflected by the variations in phonon vibration modes. As nondestructive probe techniques, Raman scattering and infrared reflection spectra can offer information on molecular polarizability, internal strain, and lattice vibrations.[38] They can also describe information on internal and external lattice vibrations caused by impurities or lack of base cations.[39] Especially, the polarized Raman scattering is considered as a reliable method to determine lattice anisotropy and symmetry.[40] This is because phonon modes will have different lattice vibration intensity in parallel-polarized (VV) and cross-polarized (VH) configuration. The Raman scattering has been successfully used as a pivotal tool to study structural phase transition according to the change in their phonon modes in extreme environments in our previous work.[12,33,38,41,42] Nevertheless, the Raman and infrared spectra under different pressure fields are desirable for estimating the phase transition process of the KNN-LN system, which can be helpful for designing and obtaining giant piezoelectric performance.

In this work, the pressure- and temperature-induced structural phase diagram of KNN-LN crystals from Raman

https://doi.org/10.1021/acsami.2c13669
ACS Appl. Mater. Interfaces 2022, 14, 45590−45599

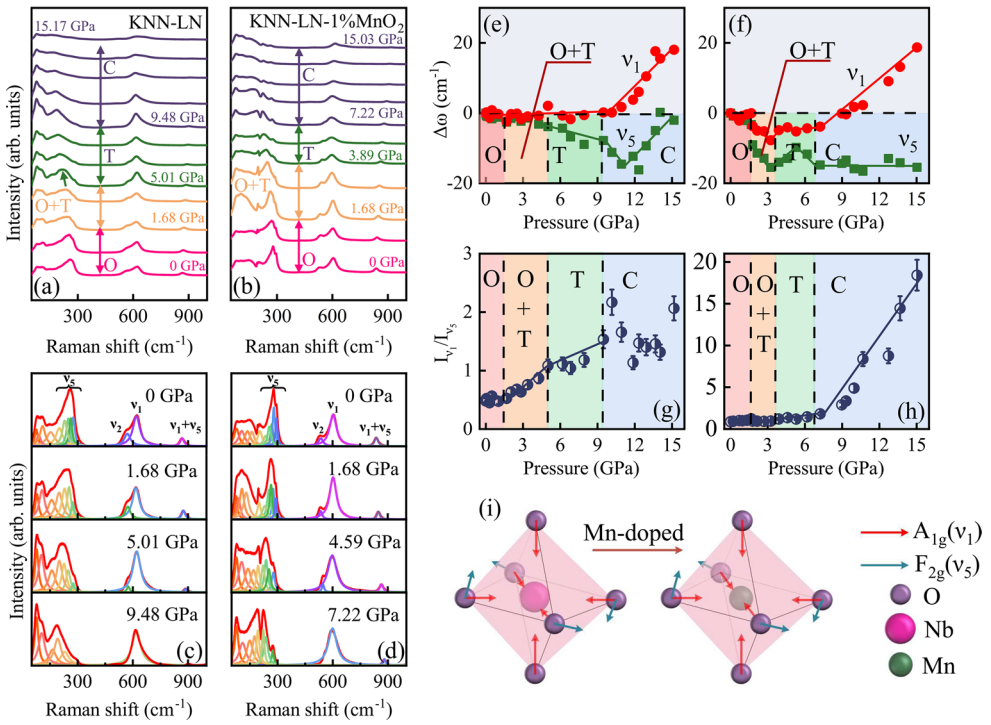

Figure 2. (a) Representative pressure-dependent Raman spectra of KNN-LN single crystals in the range from 0 to 15.17 GPa. (b) Representative pressure-dependent Raman spectra of KNN-LN-1%MnO_2 single crystals in the range from 0 to 15.03 GPa. Representative Lorentzian-shape deconvolution of Raman spectra at four selected pressures for (c) KNN-LN and (d) KNN-LN-1%MnO_2 single crystals, respectively. Pressure-dependent relative Raman shift of $F_{2g}(\nu_5)$, $A_{1g}(\nu_1)$ modes from (e) KNN-LN and (f) KNN-LN-1%MnO_2 crystals, respectively. The I_{ν_1}/I_{ν_5} ratio versus pressure has been shown for (g) KNN-LN and (h) KNN-LN-1%MnO_2 crystals, respectively. The parameters I_{ν_1} and I_{ν_5} are the intensity for the $A_{1g}(\nu_1)$ and $F_{2g}(\nu_5)$ bands from the Raman spectra of KNN-LN and KNN-LN-1%MnO_2 crystals. (i) Schematic diagrams showing the main internal vibrations of the BO_6 oxygen octahedra of the stretching $A_{1g}(\nu_1)$ mode and the bending $F_{2g}(\nu_5)$ mode.

scattering and infrared reflectance measurements was proposed. The high-pressure Raman and infrared reflection spectra of KNN-LN were compared with the results of the calculated static energy and X-ray diffraction (XRD) pattern. In addition, the effects of Mn ions substitution on the pressure critical point of KNN-LN phase transition by adding 1% MnO_2 to KNN-LN were investigated. According to the analysis of Raman shift, intensity and full width of half maximums (fwhm) in the behavior of VV and VH polarized scattering geometric phonon modes under increasing temperature from 90 to 800 K, the critical temperature point of the phase transition can be determined. After calculating the phase content at different temperature points, the more accurate phase transition critical point can also be derived. This work presents a pressure- and temperature-induced structural phase diagram, which would further improve the understanding of the physical structure characteristics and provide physical basis analysis for the future research of piezoelectric properties in high-pressure KNN-based systems.

RESULTS AND DISCUSSION

The XRD patterns from KNN-LN with different static energy (O, T, and C phases) are shown in Figure 1d. The KNN-LN crystal structure belongs to the O phase at atmospheric pressure. The main signals are from (100) and (001) orientation, which are located at 20.65 and 21.85°, respectively. As the pressure increases to 5 GPa, the KNN-LN crystal transforms to T phase, with the main signals from (200) and (110) orientation located at 30.25° and 31.10°. Note that the difference between O and T phase in the XRD patterns predicted by the CALYPSO method is not obvious. The detailed analysis of the O-T phase boundary needs to be clarified in subsequent measurements. Four XRD peaks in the O and T phase are overlapped into the signal (001) and (110) orientation in the C phase, which are located at 21.60 and 30.75°, respectively. The static energy of the different structures increase from −7.6437 to −6.0665 eV/atom according to the theoretical analysis with increasing the pressure. The CALYPSO code was used to search the global crystal structure and the phase with the lowest energy corresponding to different pressures could be found.[43] It can be concluded that the KNN-LN crystal structure undergoes O → T → C phase transformation under a high-pressure field.

In order to verify the consistency of theoretical prediction and experiment, we discussed the high-pressure Raman spectroscopy. Figure 2a, b shows pressure-dependent Raman spectra of KNN-LN and KNN-LN-1% MnO_2 in the range from 0 to 15 GPa, respectively. It can be seen that there are noticeable differences between Raman spectra of KNN-LN and KNN-LN-1% MnO_2 at 0 GPa. With increasing the pressure, the intensity of all the major peaks takes on an overall downward trend. The phase transition between the T and C phases can be determined by analyzing the change in the Raman phonon mode located at about 300 cm^{-1}. The pressure point of the KNN-LN transition from T to C phase is 9.48 GPa, while that from the KNN-LN-1%MnO_2 is lower and located at about 7.22 GPa. In order to analyze the specific discrepancy of phonon modes with the pressure, we reveal in Figure 2c, d a Lorentzian-shape decomposition for four selected pressures (0, 1.68, 5.01, and 9.48 GPa for KNN-LN

https://doi.org/10.1021/acsami.2c13669
ACS Appl. Mater. Interfaces 2022, 14, 45590−45599

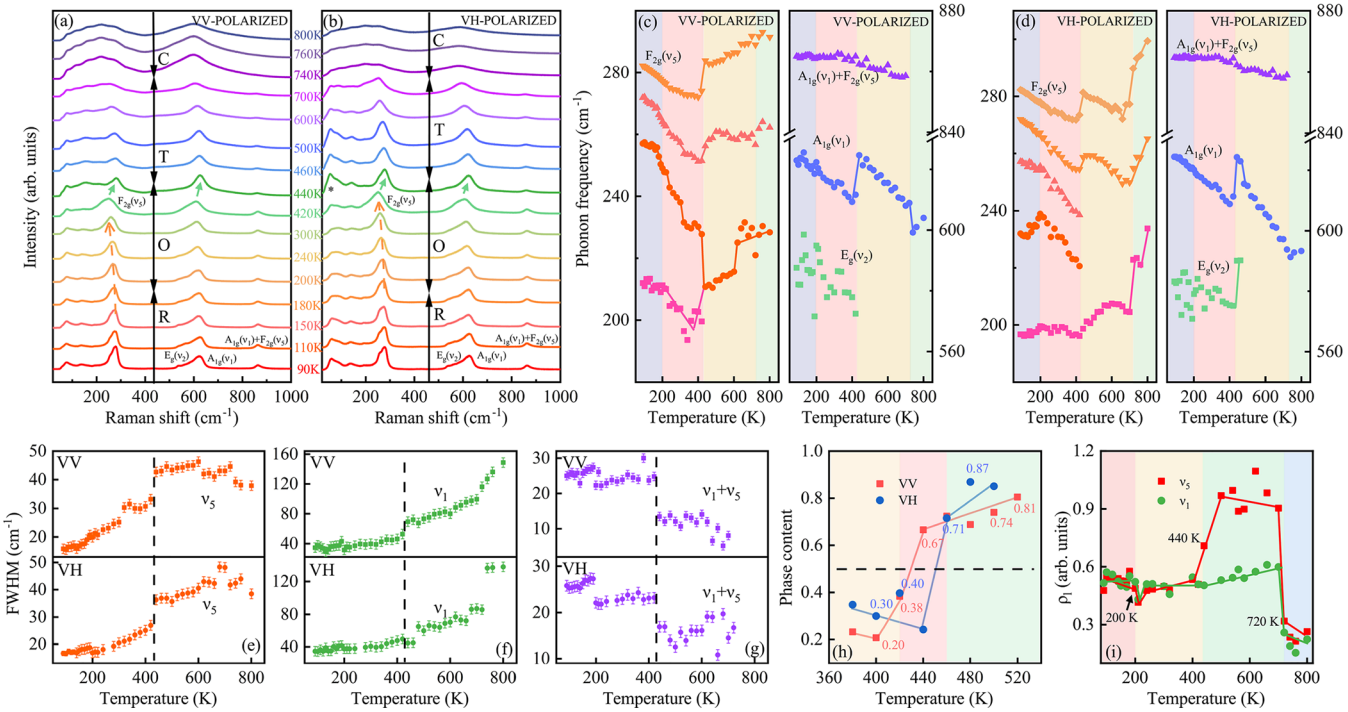

Figure 3. (a) Parallel-polarized (VV) and (b) cross-polarized (VH) Raman spectra of KNN-LN single crystals recorded in a temperature range of 90−800 K, respectively. Note that the variations from several typical lattice vibrations and the corresponding phase transitions can be remarked from the phonon frequency shift. Temperature-dependent evolution of the typical phonon frequency derived from (c) the VV configuration and (d) the VH configuration of KNN-LN single crystals, respectively. Note that the abrupt changes can be easily observed and remarked by different color filling. Temperature-dependent fwhm values under the VV and VH configurations for the (e) $F_{2g}(\nu_5)$, (f) $A_{1g}(\nu_1)$, and (g) $A_{1g}(\nu_1) + F_{2g}(\nu_5)$ modes from KNN-LN crystals, respectively. (h) Calculated r values of O → T phase transition under a temperature range of 380−520 K for KNN-LN single crystals. (i) Temperature dependence of depolarization ratio from KNN-LN crystals of polarized scattering for ν_1 and ν_5 modes.

and 0, 1.68, 4.59, and 7.22 GPa for KNN-LN-1% MnO_2), respectively. It can be observed that the Raman spectra change obviously under high pressure. The number of phonon modes decreases with increasing pressure. The phonon modes in the range of 200−300 cm^{-1} are annihilated or merged. This phenomenon is well consistent with the theoretical calculation.

Generally, a perfect NbO_6 octahedron has six phonon vibrations: the symmetric stretching mode $A_{1g}(\nu_1)$, asymmetric stretching modes $E_g(\nu_2)$ and $F_{1u}(\nu_3)$, asymmetric bending mode $F_{1u}(\nu_4)$, symmetric bending mode $F_{2g}(\nu_5)$, and the inactive mode $F_{2u}(\nu_6)$.[44,45] The ν_1, ν_2, and ν_5 modes have Raman scattering activity among these vibrations. The whole vibrational configuration can be regarded as the translational mode of basic ions and the rotational mode of the NbO_6 octahedron in the frequency range below 200 cm^{-1}.[41] MnO_2-doped KNN-LN has more splitting peaks at the phonon frequency between 200 and 300 cm^{-1}, which are related to the bending vibration of the Nb−O bond in the oxygen octahedron. The stretching modes at 619 and 566 cm^{-1} were identified as $A_{1g}(\nu_1)$ and $E_g(\nu_2)$ modes of the NbO_6 octahedron, respectively. The peak centered at 868 cm^{-1}, which nearly disappeared in the C phase, is the coupling mode of $A_{1g}(\nu_1)$ and $F_{2g}(\nu_5)$.[46] Comparing the fitting results of Figure 2c and d, KNN-LN-1%MnO_2 has more splitting peaks under the ν_5 mode. This is because Mn substitution reduces the overall symmetry of the BO_6 structure and increases the types of bending vibration modes.

Panels e and f in Figure 2 give an overview pressure evolution of relative Raman shift for two different modes (ν_1, ν_5) from 0 to 15 GPa. Since there are many subpeaks in the ν_5 phonon modes, the area of each peak is taken into account when weighting the whole ν_5 phonon modes. Relatively obvious pressure-increased Raman spectra features can be listed as follows: (I) ν_1 has almost no displacement at first, and then moves to a higher frequency, (II) the Raman shift of ν_5 phonon modes for KNN-LN is basically unchanged in the O phase and the O-T coexistence phase; however, in the T phase, there is an obvious trend of shifting to lower frequency range; (III) the phonon modes of ν_5 for KNN-LN-1% MnO_2 gradually shift to a lower frequency with increasing pressure in the O-T coexistence phase, except for a sudden shift to higher frequency in the T phase; and (IV) ν_1 exhibits a larger shift than ν_5 in the C phase, which indicates A_{1g} is more sensitive to high pressure. The irregular changes in the Raman phonon modes can be attributed to the structural phase transition T → C, which is consistent with the theoretical prediction. The phonon modes in the vicinity of the T-C phase change drastically. It means that there may be a narrow pressure range for the T-C coexistence phase. However, the phase transition between the O and T phases with multiphase coexistence is difficult to determine by Raman shifts. In order to discover more details in the variations of typical phonon modes, we can observe pressure-increase changes in KNN-LN and KNN-LN-1% MnO_2 by Raman spectral characteristics, such as intensity and full width of half maximum (fwhm). The fwhm and scattering intensity are of great significance for the study of the off-center displacement of the B-site cations.[47] However, the off-center displacement of cations at the A-site and the B-site are the essence of the spontaneous polarization of displacive ferroelectric materials, while high pressure is

https://doi.org/10.1021/acsami.2c13669
ACS Appl. Mater. Interfaces 2022, 14, 45590−45599

beneficial to BO_6 tilting[48] and reduces eccentric displacement of the B-site cation. Figure 3g, h display the intensity of the $A_{1g}(\nu_1)/F_{2g}(\nu_5)$ ratio versus pressures. The competition between the two phonon modes can be clearly obtained, especially for the variation with increasing pressure. The intensity ratio of KNN-LN has fewer changes under 1.68 GPa, indicating that pressure has relatively less effect on the O phase. In the O-T coexistence phase, the $A_{1g}(\nu_1)/F_{2g}(\nu_5)$ ratios of KNN-LN have an upward tendency. The stretching $A_{1g}(\nu_1)$ mode gradually becomes dominant, while the intensity of the bending $F_{2g}(\nu_5)$ mode is decreasing, which means that the off-center displacement of the B-site cations will be repressed by high pressure. Therefore, the pressure point for the O-T coexistence phase boundary located at about 1.68−5.01 GPa can be obtained from the sharp change in the intensity ratio. Moreover, there is a considerable difference between KNN-LN and KNN-LN-1% MnO_2 crystals when they transform to T phase. On the other hand, we can also conclude that the intensity ratio of KNN-LN-1%MnO_2 increases sharply in the C phase. This phenomenon is significantly more dramatic than the changing trend of KNN-LN without the Mn introduction. In general, the cubic perovskite phase does not support the active Raman modes, with all ions in the inversion centers. Hence, the Raman signal in C phase indicates that the phase has a significant local deviation from the cubic structure.[49] The effect from the substitution of Mn ions on the high-pressure C phase need to be further investigated.

Figure 2i describes the schematic diagram for directions of molecular vibration intuitively. The orientation of stretching $A_{1g}(\nu_1)$ mode is parallel to the interaction direction between oxygen and Nb ions, while the direction of $F_{2g}(\nu_5)$ is perpendicular to them. In the internal modes of the NbO_6 octahedron, the bond length become shorter with the smaller Mn ion substitution instead of larger Nb ions. The doping of MnO_2 will change the interaction between oxygen and the B-site, inducing a greater influence on the structural variation. It causes additional octahedral distortion and promotes the development of octahedral tilt.[50] Hence, the substitution of Mn ions propelled the ABO_3 structure toward the cubic aristotype, which aggravates the deformation of high pressure on KNN-LN and promotes its phase transition earlier. The Mn ions replace the A- or B-sites as electrons or holes for absorption. The substitution of the A-site requires the reduction of Nb ions and promotes the formation of free electrons, resulting in an increase in holes. The oxidation process of B-site substitution can inhibit the increase in holes by filling them, which is a useful method of Mn substitution to reduce leakage current. In the ABO_3 structure, the bond length of the A−O bond is longer than that of the B−O bond. The B−O bonds stretch while the A−O bonds compress during the process of the ABO_3 structure transforming into a cubic structure.[51] Therefore, the B−O bond of the ABO_3 structure is easier to compress under an external pressure field. Similarly, the substitution of Mn at the B-site can promote octahedral compression, as compared to that at the A-site. Here we refer to the concept of tolerance factor τ to further illustrate the role of Mn substitution, defined as $\tau = r_{A-O}/\sqrt{2}(r_{B-O})$. r_{A-O} and r_{B-O} represent A−O and B−O bond lengths, respectively.[52] The ABO_3 structure in the C phase has lattice constants of $a = b = c$, and hence the τ value is 1.[53] Due to the compressibility of the B−O bond, the Mn doping will reduce r_{B-O} and increase the τ value, approaching 1. Thus, the structure is closer to a cubic phase with the smaller rotation amplitude of the octahedron. The changes in the B−O bond length and tolerance factor illustrate that the Mn substitution promotes the phase transition from the T to C phase.

The polarized Raman scattering is a unique method for determining lattice symmetry. In the thermal field, phase transitions can be judged by using abnormal variations in frequency after the thermal effects on the lattice were eliminated. The thermal evolution results collected from temperature-dependent Raman spectra with two polarized scattering geometry [VV and VH] can accurately reveal the phase transitions of O to T to C phases. Figure 3a, b displays the evolution of VV and VH polarized Raman spectra with the temperature varying from 90 to 800 K. The previous research show that the KNN-LN crystal structure transforms from O to T and C phases with the temperature increasing from room temperature to high temperature.[12] On this basis, the structural variation at lower temperature was additionally studied. As plotted in Figure 3a, b, with the fitting results in Figure 3c, d, the $F_{2g}(\nu_5)$ phonon modes slowly shift to lower frequency in the low-temperature range below 200 K. The frequency drops rapidly after the temperature goes beyond 200 K. Therefore, KNN-LN can transform to the rhombohedral (R) phase with an *R3m* space group at low temperature, which is consistent with the other studies.[54,55] On the other hand, there is a significant reversal at about 420 K, wherein almost all phonon modes have a blueshift trend. The anomalous blueshift indicates the O to T phase transition. In the temperature range below 420 K, all the phonon modes have a redshift trend in both VV and VH configurations. The effect of thermal expansion on the lattice will cause the redshift of the phonon frequency, and the reduction of optical phonon energy can also promote it. A new phonon mode at about 50 cm^{-1} can be found with the temperature beyond 420 K in the VH configuration labeled (*). The frequency of the ν_1 and ν_5 coupling mode the phenomenon of shifting toward the high wavenumber region shown in the pressure-dependent experiment, and it is relatively stable on the whole with a slight red shift. It is mainly the vibration of oxygen ions in the Nb−O plane,[56] which is not as sensitive to temperature as to pressure. The phonon modes below 200 cm^{-1} are related to the translational mode of cations, which are highly sensitive to the polarized orientation. The phonon mode located at about 232 cm^{-1} under the VH configuration shows an abnormal blueshift, whereas it cannot be observed readily from the VV configuration. Hence, the bending vibration of the Nb−O bond has different sensitivity from the VV and VH configuration.

Figure 3e−g shows the fwhm variation of the $F_{2g}(\nu_5)$, $A_{1g}(\nu_1)$, and $\nu_1+\nu_5$ phonon modes versus temperature. Except for the general upward trend in a single phase, the fwhm value of the $A_{1g}(\nu_1)$ mode is larger than that of $F_{2g}(\nu_5)$ mode in the whole temperature range. The fwhm data remain almost relatively constant at low temperature. With increasing the temperature above 200 K, it begins to rise rapidly. This is similar to the change of the frequency shift, indicating the phase transition pattern. Another interesting phenomenon occurs at a temperature of about 420 K, where the fwhm value of $F_{2g}(\nu_5)$ mode and $A_{1g}(\nu_1)$ mode have a noteworthy discontinuous change. However, the $\nu_1+\nu_5$ phonon modes have a significant reduction. As we know, the particularity of piezoelectric properties near the thermotropic phase boundaries is significant. As one of the important characteristics of first-order phase transition, the mixture of O and T phases has

https://doi.org/10.1021/acsami.2c13669
ACS Appl. Mater. Interfaces 2022, 14, 45590−45599

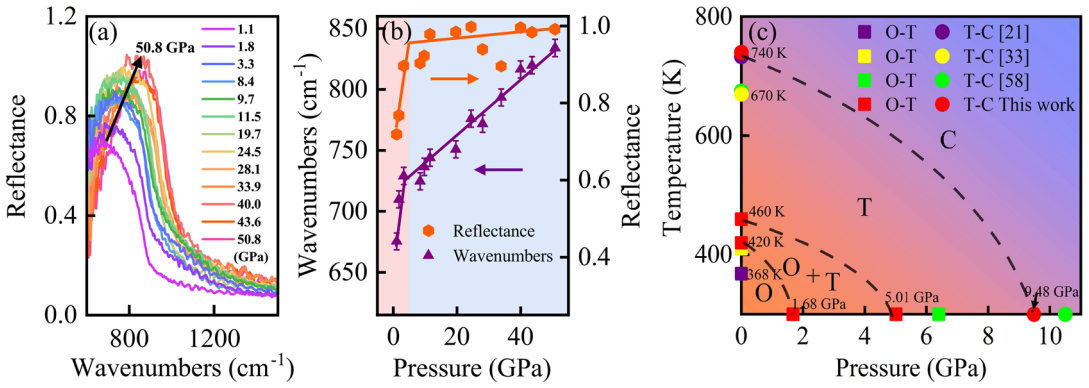

Figure 4. (a) Infrared reflectance spectra of KNN-LN single crystals under a pressure range of 1.1−50.8 GPa at room temperature. (b) Phonon frequency of the $F_{1u}(\nu_3)$ mode and the maximum reflectivity versus pressure present abrupt variation. (c) Schematic temperature- and/or pressure-dependent phase diagram of KNN-LN single crystals derived from the critical pressures and temperatures identified. The values in this work are indicated by red squares and circle on the coordinate axis while the other signals represent the published works from the listed references. Phase boundaries with their uncertainties are represented by the dashed lines.

been found at the phase boundary in our previous study.[10] An assumption was established[12] that the spectra near the phase boundaries are linearly superimposed to obtain the phase on the thermal phase boundaries. The coexistence of the O phase and the T phase on the thermal phase boundary was confirmed by the basic anastomosis between the experimental data and the formula: $I = (1 - r)I_- + rI_+$ (I is the fitted Raman spectra, I_- and I_+ represent Raman spectra below and above thermal phase boundary, $0 < r < 1$). The intensity of polarization Raman scattering is related to molecular symmetry and anisotropy, which is proportional to the polarization.[42] In order to accurately determine the O-T phase transition temperature, we show the r values of the temperature from 380 to 520 K in Figure 3h. The area of all Raman signals was normalized to exclude the influence of external factors on the laser intensity. The intensity values at temperatures of 300 and 600 K are determined as O phase and T phase respectively as I_- and I_+. As shown in Figure 3h, in the temperature range of 420−460 K, the content of the T phase of the VV configuration increases sharply from 0.38 to 0.67 and from 0.40 to 0.71 for the VH configuration, respectively. The coexistence value illustrates that the O-T phase transition has a slight temperature difference between the VV and VH configurations, and there exists a region where the O and T phases coexist near 440 K.

The anomalous polarization scattering intensity near the phase transition point reflects the symmetry variation and rearrangement. The depolarization ratio ($\rho_l = I_{VH}/I_{VV}$) would distinguish the phonon configurations and lattice structure evolution of KNN-LN. Figure 3i indicates the depolarization ratio of vibrational modes of $F_{2g}(\nu_5)$ mode and $A_{1g}(\nu_1)$ in the temperature range of 90−800 K. The temperatures of symmetry breaking on KNN-LN are around 200, 440, and 720 K. The sudden drop of the $F_{2g}(\nu_5)$ mode at the temperature point of 720 K is obvious, as is the continuous rise at 440 K. Differently, the depolarization ratio of the $A_{1g}(\nu_1)$ mode around 440 K becomes stable. In the C phase, the KNN-LN crystal has a cubic structure with high lattice symmetry. Therefore, ρ_l of both the $A_{1g}(\nu_1)$ and $F_{2g}(\nu_5)$ modes decreases significantly after the crystal transforms to the C phase, which indicates the enhancement of symmetry and the discontinuity of phase transition. The depolarization ratio plays a significant role in the evolution study of lattice symmetry.

In addition to the Raman active modes $A_{1g}(\nu_1)$, $E_g(\nu_2)$, and $F_{2g}(\nu_5)$, the NbO_6 octahedron also has infrared-active $F_{1u}(\nu_3)$ and $F_{1u}(\nu_4)$ modes with more lattice details. Figure 4a depicts the infrared reflectance spectra of KNN-LN crystal under different pressure fields. The high-reflectance region of 660−840 cm^{-1} is associated with the $F_{1u}(\nu_3)$ mode, which is related to the Nb−O stretching mode.[57] The peak position and reflectance intensity are obtained by the Lorentz fitting, as shown in Figure 4b. It was found that the change of peak position and strength is more obvious in the pressure range of 1.10−3.30 GPa. The abnormal change in infrared reflectance intensity is consistent with the results from Raman spectroscopy, which verifies the existence of the O-T phase coexistence near this pressure point. Therefore, the sharp change in infrared reflectance intensity in the range below 3.30 GPa corresponds to the O-T phase transition result, which has been already obtained by Raman scattering. Moreover, the previous pressure-dependent Raman analysis shows the phonon mode competition between $A_{1g}(\nu_1)$ and $F_{2g}(\nu_5)$. It was concluded that the stretching mode $A_{1g}(\nu_1)$ gradually dominates in the T phase with increasing pressure. Thus, the phase transition process can also be analyzed by the infrared reflectance spectra.

In order to further analyze the relationship between temperature- and pressure-dependent phase transition, we show a schematic temperature and/or pressure phase diagram in Figure 4c. Temperature−composition phase diagrams have been already studied for $(1 - x)$KNN-xLN solid solution by Klein et al.[21] The data with $x = 5\%$ have been selected and marked it with purple squares and circles in Figure 4c. In addition, the yellow and green markers were selected from the temperature-dependent experiment of Mn-doped KNN-$LiBiO_3$ and the calculated phase transition points of KNN, respectively.[33,58] The phase boundary under high temperature and pressure with the dotted lines was indicated. The KNN-LN transforms from the O phase to the T and C phase with the temperature or pressure increasing, while the space group follows the transition sequence of $Amm2 \rightarrow P4mm \rightarrow Pm3m$. The effect of thermal expansion during the heating process and volume contraction as pressure increases on KNN-LN volume are opposite.[52] Due to the compressibility of BO_6 structure,[42,51] the thermal expansion phenomenon with increasing temperature cannot offset the volume shrinkage caused by phase transition. Besides, by increasing the pressure acting on

https://doi.org/10.1021/acsami.2c13669
ACS Appl. Mater. Interfaces 2022, 14, 45590−45599

KNN-LN, the energy of KNN-LN increases while the stability decreases from the theoretical calculation, so the entropy $\Delta S > 0$ during the phase transition. Therefore, entropy (S) and volume (V) change are positive and negative ($\Delta S > 0$, $\Delta V < 0$), which cause the compressible BO_6 octahedral perovskite to exhibit negatively inclined phase boundaries in the temperature−pressure phase diagram generally.[37] Therefore, although there is a lack of a phase transition critical point and an uncertainty of the phase boundary in a high-temperature and -pressure environment, one can still assume that KNN-LN has similar negatively inclined phase boundaries. Moreover, the final phase diagram obtained by the optical spectroscopy is well consistent with the structure at 0, 5, and 20 GPa derived by the theoretical predictions, which belong to O, T, and C phases, respectively. These data can improve further insight on the piezoelectric performance of a KNN-based system.

CONCLUSIONS

In summary, we systematically investigated the features of pressure-dependent and polarized temperature-dependent phonon behaviors in KNN-LN crystals. The O-T and T-C phase transition pressure points of KNN-LN were observed at 1.68−5.01 and 9.48 GPa under the stress field, which is in agreement with the phase structures predicted by the CALYPSO method at different pressures. The analysis of competition between the $A_{1g}(\nu_1)$ and $F_{2g}(\nu_5)$ phonon vibration modes and infrared reflectance spectra supported the conclusion that the stretching mode $A_{1g}(\nu_1)$ gradually dominates in the T phase. As a comprehensive additive, the doping of MnO_2 causes Mn ions to replace the A- or B-sites of NbO_6 structure, in which the B-site substitution is dominant, encouraging the phase transition of KNN-LN from T to C phase at lower pressure points. In addition to analyzing the polarized temperature-dependent Raman shift, the scattering intensity, and fwhm to infer the phase transition points among the O, T, and C phases, the coexistence value (r) was calculated at temperature points near the O-T phase boundary (420−460 K) in order to study the phase competition and phase coexistence. The phase diagram can comprehensively display the results on KNN-LN. Both temperature and pressure can add energy to the system and increase entropy; the compressible BO_6 octahedral perovskite usually presents a negative inclined phase boundary in the temperature and/or pressure phase diagram. This work will be helpful for future research on the structure properties in KNN-based crystals and the development of lead-free piezoelectric systems.

EXPERIMENTAL SECTION

Preparation of KNN-LN and KNN-LN-1%MnO_2 single Crystal Samples. $(K_{0.5}Na_{0.5})NbO_3$-0.05$LiNbO_3$-γMnO_2 (γ = 0 and 1.0%) single crystals were grown by the flux-Bridgman method. The specific preparation process was reported previously.[59]

CALYPSO Method. The CALYPSO (crystal structure analysis by particle swarm optimization) method is an efficient method for crystal structure prediction. It only needs the chemical composition of a compound to predict a stable or metastable structure under given external conditions. It can generate a number of test structures in a predefined unit cell before simulating the diffraction pattern of each test structure.[60−62] Structural searches were performed using models consisting of four formula units at 0, 5, and 20 GPa. First-generation structures are randomly generated, then optimized and evolved into the next generation. Twenty generations were subsequently followed, each containing 50 structures, to obtain the most stable structures. Moreover, locally structure optimization techniques are used to obtain a local minimum of lattice energy.

Pressure-Dependent Raman Scattering Measurements. Raman scattering measurements were performed with Jobin-Yvon LabRAM HR Evolution spectrometer. A laser with the wavelength of 532 nm and a 1800 grooves/mm grating was taken as the excitation source and the spectral resolution is better than 1 cm^{-1}. The laser was focused on the sample through a 50× microscope with a working distance of 18 mm. For high-pressure experiments, we have used a Mao-Bell-type diamond anvil cell (DAC) with two 300 μm culet diamonds and a stainless steel gasket. The specific structure diagram of DAC was plotted in Figure 1b. Silicone oil was used as a pressure-transmitting medium. The ruby luminescence method was used to calibrate the pressure value.[63,64]

Polarized Temperature-Dependent Raman Scattering Measurements. Linkam THMSE 600 heating/cooling stage, with a temperature rate of 10 K/min, was used in temperature-dependent Raman experiment. In order to eliminate the contribution of the Raman spectra to the Bose−Einstein temperature factor, we reduced all the spectra by $n(\omega, T) + 1$. The Bose−Einstein temperature factor is obtained by $n(\omega, T) = 1/[\exp(\hbar\omega/kT) - 1]$ ($\hbar$ and ω represent the reduced Planck constant and the phonon frequency, while k and T represent the Boltzmann constant and the temperature). Polarizers were placed in the excitation and detection paths to define VV and VH scattering geometries in polarized scattering measurements.

Infrared Reflectance Spectra. Infrared reflectance spectra were implemented by the FTIR spectrometer (Bruker, Vertex 70v). The microscope (Hyperion 2000) was equipped with a nitrogen-cooled MCT detector. A gold mirror was utilized as a reference to the reflectivity between the transmitting medium and the culet of the diamond anvil. Note that no mathematical smoothing was performed for the experimental reflectance data.

AUTHOR INFORMATION

Corresponding Authors

Kai Jiang − *Technical Center for Multifunctional Magneto-Optical Spectroscopy (Shanghai), Engineering Research Center of Nanophotonics & Advanced Instrument (Ministry of Education), Department of Physics, School of Physics and Electronic Science, East China Normal University, Shanghai 200241, China*; Email: kjiang@ee.ecnu.edu.cn

Zhigao Hu − *Technical Center for Multifunctional Magneto-Optical Spectroscopy (Shanghai), Engineering Research Center of Nanophotonics & Advanced Instrument (Ministry of Education), Department of Physics, School of Physics and Electronic Science, East China Normal University, Shanghai 200241, China; Collaborative Innovation Center of Extreme Optics, Shanxi University, Taiyuan, Shanxi 030006, China*; orcid.org/0000-0003-0575-2191; Email: zghu@ee.ecnu.edu.cn

Authors

Yuting Yan − *Technical Center for Multifunctional Magneto-Optical Spectroscopy (Shanghai), Engineering Research Center of Nanophotonics & Advanced Instrument (Ministry of Education), Department of Physics, School of Physics and Electronic Science, East China Normal University, Shanghai 200241, China*

Anyang Cui − *Technical Center for Multifunctional Magneto-Optical Spectroscopy (Shanghai), Engineering Research Center of Nanophotonics & Advanced Instrument (Ministry of Education), Department of Physics, School of Physics and Electronic Science, East China Normal University, Shanghai 200241, China*

Kai Dai − *Technical Center for Multifunctional Magneto-Optical Spectroscopy (Shanghai), Engineering Research*

https://doi.org/10.1021/acsami.2c13669
ACS Appl. Mater. Interfaces 2022, 14, 45590−45599

Center of Nanophotonics & Advanced Instrument (Ministry of Education), Department of Physics, School of Physics and Electronic Science, East China Normal University, Shanghai 200241, China

Yan Ye − *Technical Center for Multifunctional Magneto-Optical Spectroscopy (Shanghai), Engineering Research Center of Nanophotonics & Advanced Instrument (Ministry of Education), Department of Physics, School of Physics and Electronic Science, East China Normal University, Shanghai 200241, China*

Jinzhong Zhang − *Technical Center for Multifunctional Magneto-Optical Spectroscopy (Shanghai), Engineering Research Center of Nanophotonics & Advanced Instrument (Ministry of Education), Department of Physics, School of Physics and Electronic Science, East China Normal University, Shanghai 200241, China;* orcid.org/0000-0003-1511-4281

Jiajia Feng − *Center for High Pressure Science and Technology Advanced Research, Shanghai 201203, China*

Hongliang Dong − *Center for High Pressure Science and Technology Advanced Research, Shanghai 201203, China*

Complete contact information is available at: https://pubs.acs.org/10.1021/acsami.2c13669

Author Contributions

The manuscript was written through contributions of all authors. All authors have given approval to the final version of the manuscript.

Notes

The authors declare no competing financial interest.

■ ACKNOWLEDGMENTS

The authors acknowledge the assistance of Prof. Guisheng Xu (Shanghai Institute of Ceramics, Chinese Academy of Sciences) in sample preparation. This work was financially supported by the National Natural Science Foundation of China (Grants 62090013, 61974043, 12104156, 62074058, and 91833303), the National Key R&D Program of China (Grants 2019YFB2203403), the Projects of Science and Technology Commission of Shanghai Municipality (Grants 21JC1402100 and 19511120100), China Postdoctoral Science Foundation (Grants 2020TQ0099 and 2020M681222), the Program for Professor of Special Appointment (Eastern Scholar) at Shanghai Institutions of Higher Learning, and Shanghai Pujiang Program (20PJ1403600).

■ REFERENCES

(1) Saito, Y.; Takao, H.; Tani, T.; Nonoyama, T.; Takatori, K.; Homma, T.; Nagaya, T.; Nakamura, M. Lead-free Piezoceramics. *Nature (London)* **2004**, *432*, 84−87.

(2) Rubio-Marcos, F.; López-Juárez, R.; Rojas-Hernandez, R. E.; Del Campo, A.; Razo-Pérez, N.; Fernandez, J. F. Lead-Free Piezoceramics: Revealing the Role of the Rhombohedral-Tetragonal Phase Coexistence in Enhancement of the Piezoelectric Properties. *ACS Appl. Mater. Interfaces* **2015**, *7*, 23080−23088.

(3) Zhang, S. J.; Xia, R.; Shrout, T. R.; Zang, G. Z.; Wang, J. F. Piezoelectric Properties in Perovskite $0.948(K_{0.5}Na_{0.5})$-NbO_3C0.052$LiSbO_3$ Lead-free Ceramics. *J. Appl. Phys.* **2006**, *100*, 104108.

(4) Tashiro, S.; Nagamatsu, H.; Nagata, K. Sinterability and Piezoelectric Properties of $KNbO_3$ Ceramics after Substituting Pb and Na for K. *Jpn. J. Appl. Phys.* **2002**, *41*, 7113−7118.

(5) Liu, H.; Liu, Y. X.; Song, A. Z.; Li, Q.; Yin, Y.; Yao, F. Z.; Wang, K.; Gong, W.; Zhang, B. P.; Li, J. F. (K, Na)NbO_3-based Lead-free Piezoceramics: One more Step to Boost Applications. *Nati. Sci. Rev.* **2022**, *9*, nwac101.

(6) Huangfu, G.; Xiao, H. Y.; Guan, L.; Zhong, H. Y.; Hu, C.; Shi, Z. W.; Guo, Y. P. Visible or Near-Infrared Light Self-Powered Photodetectors Based on Transparent Ferroelectric Ceramics. *ACS Appl. Mater. Interfaces* **2020**, *12*, 33950−33959.

(7) Liu, Y.; Xu, G. S.; Liu, J. F.; Yang, D. F.; Chen, X. X. Dielectric, Piezoelectric Properties of MnO_2-doped $(K_{0.5}Na_{0.5})$-NbO_3C0.05$LiNbO_3$ Crystal Grown by Flux-Bridgman Method. *J. Alloys Compd.* **2014**, *603*, 95−99.

(8) Zhang, S. J.; Xia, R.; Shrout, T. R. Modified $(K_{0.5}Na_{0.5})NbO_3$ Based Lead-free Piezoelectrics with Broad Temperature Usage Range. *Appl. Phys. Lett.* **2007**, *91*, 132913.

(9) Hao, J. G.; Li, W.; Zhai, J. W.; Chen, H. Progress in High-strain Perovskite Piezoelectric Ceramics. *Mater. Sci. Eng. R* **2019**, *135*, 1−57.

(10) Cui, A. Y.; Jiang, K.; Zhang, P.; Xu, L. P.; Xu, G. S.; Chen, X. M.; Hu, Z. G.; Chu, J. H. In Situ Exploration of Thermal-Induced Domain Evolution with Phase Transition in $LiNbO_3$-Modified $K_{0.5}Na_{0.5}NbO_3$ Single Crystal. *J. Phys. Chem. C* **2017**, *121*, 14322−14329.

(11) Dai, Y. J.; Zhang, X. W.; Zhou, G. Y. Phase Transitional Behavior in $K_{0.5}Na_{0.5}NbO_3$−$LiTaO_3$ Ceramics. *Appl. Phys. Lett.* **2007**, *90*, 262903.

(12) Xu, L. P.; Jiang, K.; Zhang, J. Z.; Xu, G. S.; Hu, Z. G.; Chu, J. H. Phase Transitions and Thermotropic Phase Boundaries in MnO_2-doped $(K_{0.5}Na_{0.5})NbO_3$-0.05$LiNbO_3$ Single Crystals: Raman Scattering Evidence at Elevated Temperatures. *Appl. Phys. Lett.* **2015**, *106*, 122901.

(13) Shirane, G.; Danner, H.; Pavlovic, A.; Pepinsky, R. Phase Transitions in Ferroelectric $KNbO_3$. *Phys. Rev.* **1954**, *93*, 672−673.

(14) Rubio-Marcos, F.; Del Campo, A.; López-Juárez, R.; Romero, J. J.; Fernández, J. F. High Spatial Resolution Structure of (K,Na)NbO_3 Lead-free Ferroelectric Domains. *J. Mater. Chem.* **2012**, *22*, 9714−9720.

(15) Zheng, T.; Wu, H. J.; Yuan, Y.; Lv, X.; Li, Q.; Men, T. L.; Zhao, C. L.; Xiao, D. Q.; Wu, J. G.; Wang, K.; Li, J. F.; Gu, Y. L.; Zhu, J. G.; Pennycook, S. J. The Structural Origin of Enhanced Piezoelectric Performance and Stability in Lead Free Ceramics. *Energy Environ. Sci.* **2017**, *10*, 528−537.

(16) Li, P.; Zhai, J. W.; Shen, B.; Zhang, S. J.; Li, X. L.; Zhu, F. Y.; Zhang, X. M. Ultrahigh Piezoelectric Properties in Textured (K,Na)NbO_3-Based Lead-Free Ceramics. *Adv. Mater.* **2018**, *30*, 1705171.

(17) Shrout, T. R.; Zhang, S. J. Lead-free Piezoelectric Ceramics: Alternatives for PZT? *J. Electroceram.* **2007**, *19*, 113−126.

(18) Ma, C.; Guo, H. Z.; Beckman, S. P.; Tan, X. L. Creation and Destruction of Morphotropic Phase Boundaries through Electrical Poling: A Case Study of Lead-Free $(Bi_{1/2}Na_{1/2})TiO_3$-$BaTiO_3$ Piezoelectrics. *Phys. Rev. Lett.* **2012**, *109*, 107602.

(19) Tan, Z.; Xing, J.; Peng, Y. T.; Zhang, Q. M.; Zhu, J. G. Polarization Rotation Boosts Strong Piezoelectric Response in the Lead-free Perovskite Ferroelectric $K_{0.5}Na_{0.5}NbO_3$. *Phys. Rev. B* **2021**, *104*, 014104.

(20) Xiao, H. Y.; Dong, W.; Guo, Y. P.; Wang, Y. F.; Zhong, H. Y.; Li, Q.; Yang, M. M. Design for Highly Piezoelectric and Visible/Near-Infrared Photoresponsive Perovskite Oxides. *Adv. Mater.* **2019**, *31*, 1805802.

(21) Klein, N.; Hollenstein, E.; Damjanovic, D.; Trodahl, H. J.; Setter, N.; Kuball, M. A study of the Phase Diagram of (K,Na,Li)-NbO_3 Determined by Dielectric and Piezoelectric Measurements, and Raman Spectroscopy. *J. Appl. Phys.* **2007**, *102*, 014112.

(22) Kizaki, Y.; Noguchi, Y.; Miyayama, M. Defect Control for Low Leakage Current in $K_{0.5}Na_{0.5}NbO_3$ Single Crystals. *Appl. Phys. Lett.* **2006**, *89*, 142910.

(23) Lv, X.; Wu, J. G.; Yang, S.; Xiao, D. Q.; Zhu, J. G. Identification of Phase Boundaries and Electrical Properties in Ternary Potassium-Sodium Niobate-Based Ceramics. *ACS Appl. Mater. Interfaces* **2016**, *8*, 18943−18953.

(24) Tao, H.; Wu, J. G.; Zheng, T.; Wang, X. J.; Lou, X. J. New (1-x)$K_{0.45}Na_{0.55}Nb_{0.96}Sb_{0.04}O_3$ − $xBi_{0.5}Na_{0.5}HfO_3$ Lead-free Ceramics: Phase Boundary and their Electrical Properties. *J. Appl. Phys.* **2015**, *118*, 044102.
(25) Wu, J. G.; Xiao, D. Q.; Zhu, J. G. Potassium-Sodium Niobate Lead-Free Piezoelectric Materials: Past, Present, and Future of Phase Boundaries. *Chem. Rev.* **2015**, *115*, 2559−2595.
(26) Lv, X.; Wu, J. G.; Zhang, X. X. Tuning the Covalency of A-O Bonds to Improve the Performance of KNN-Based Ceramics with Multiphase Coexistence. *ACS Appl. Mater. Interfaces* **2020**, *12*, 49795−49804.
(27) Wang, K.; Li, J. F. Domain Engineering of Lead-Free Li-Modified (K,Na)NbO_3 Polycrystals with Highly Enhanced Piezoelectricity. *Adv. Funct. Mater.* **2010**, *20*, 1924−1929.
(28) Tang, W. B.; Xue, X. G.; Yuan, C. L.; Chen, J.; Miao, L.; Feng, Q.; Xu, J. W.; Rao, G. H.; Wang, J.; Zhou, C. R.; Guo, Y. P. Visible-light Photocatalytic Hydrogen Production in a Narrow-bandgap Semiconducting La/Ni-modified $KNbO_3$ Ferroelectric and Further Enhancement via High-field Poling. *J. Mater. Chem. A* **2022**, *10*, 7238.
(29) Zhang, Y.; Meng, X. D.; Huang, F.; Hu, C. P.; Tan, P.; Wang, Y.; Huang, X. L.; Zhou, Z. X.; Tian, H. Effects of Mn-doping on Anti-fatigue and Anti-leakage Current Characteristics in KNN Single Crystals. *Appl. Phys. Lett.* **2021**, *118*, 042903.
(30) Kubacki, J.; Molak, A.; Talik, E. Electronic Structure of $NaNbO_3$CMn Single Crystals. *J. Alloys Compd.* **2001**, *328*, 156−161.
(31) Zhang, Q. H.; Zhang, Y. Y.; Wang, F. F.; Wang, Y. J.; Lin, D.; Zhao, X. Y.; Luo, H. S.; Ge, W. W.; Viehland, D. Enhanced Piezoelectric and Ferroelectric Properties in Mn-doped $Na_{0.5}Bi_{0.5}TiO_3$CBaTiO_3 Single Crystals. *Appl. Phys. Lett.* **2009**, *95*, 102904.
(32) Jiang, M. H.; Zhang, J. W.; Rao, G. H.; Li, D. D.; Randall, C. A.; Li, T.; Peng, B. L.; Li, L.; Gu, Z. F.; Liu, X. Y.; Huang, H. T. Ultrahigh Piezoelectric Coefficient of a Lead-free $K_{0.5}Na_{0.5}NbO_3$-based Single Crystal Fabricated by a Simple Seed-free Solid-state Growth Method. *J. Mater. Chem. C* **2019**, *7*, 14845−14854.
(33) Cui, A. Y.; Cao, X. H.; Ye, Y.; Jiang, K.; Zhu, L. Q.; Jiang, M. H.; Rao, G. H.; Li, Y. W.; Hu, Z. G.; Chu, J. H. Phase Transitions and Phonon Thermodynamics in Giant Piezoelectric Mn-doped $K_{0.5}Na_{0.5}NbO_3$-$LiBiO_3$ Crystals Studied by Raman Spectroscopy. *Phys. Rev. B* **2020**, *102*, 214102.
(34) Wang, L. Y.; Ren, W.; Shi, P.; Wu, X. Q. Structures, Electrical Properties, and Leakage Current Behaviors of Un-doped and Mn-doped Lead-free Ferroelectric $K_{0.5}Na_{0.5}NbO_3$ Films. *J. Appl. Phys.* **2014**, *115*, 034103.
(35) Fan, X. J.; Wang, Y.; Jiang, Y. J. Structure and Electrical Properties of MnO_2-doped $Sr_{2-x}Ca_xNaNb_5O_{15}$ Lead-free Piezoelectric Ceramics. *J. Alloys Compd.* **2011**, *509*, 6652−6658.
(36) Shao, S.; Zhu, W. J.; Lv, J.; Wang, Y. C.; Chen, Y.; Ma, Y. M. The Exotically Stoichiometric Compounds in AlCS System under High Pressure. *NPJ. Comput. Mater.* **2020**, *6*, 11.
(37) Angel, R. J.; Zhao, J.; Ross, N. L. General Rules for Predicting Phase Transitions in Perovskites due to Octahedral Tilting. *Phys. Rev. Lett.* **2005**, *95*, 025503.
(38) Bian, M. Y.; Ye, Y.; Cui, A. Y.; Jiang, K.; Bai, W.; Dong, H. L.; Chen, B.; Hu, Z. G.; Chu, J. H. Phase Transition of $Bi_5Ti_3FeO_{15}$ Ceramics Discovered by Raman Spectroscopy and in situ Synchrotron XRD under Stress Field. *Appl. Phys. Lett.* **2020**, *117*, 022901.
(39) Singh, R.; Kambale, K.; Kulkarni, A.; Harendranath, C. Structure Composition Correlation in KNN-BT Ceramics - An X-ray Diffraction and Raman Spectroscopic Investigation. *Mater. Chem. Phys.* **2013**, *138*, 905−908.
(40) Klauer, S.; Wohlecke, M. Local Symmetry of Hydrogen in Cubic and Tetragonal $SrTiO_3$ and $KTaO_3$:Li Determined by Polarized Raman Scattering. *Phys. Rev. Lett.* **1992**, *68*, 3212−3215.
(41) Dai, K.; Cui, A. Y.; Ye, Y.; Jiang, K.; Zhang, J. Z.; Li, Y. W.; Wang, G. S.; Dong, X. L.; Hu, Z. G.; Chu, J. H. Phase Diagram With an Antiferroelectric/ferroelectric Phase Boundary in $AgNbO_3$-$LiTaO_3$ Energy-storage Ceramics by Lattice Dynamics and Electronic Transitions. *Phys. Rev. B* **2021**, *104*, 174104.
(42) Ye, Y.; Cui, A. Y.; Bian, M. Y.; Jiang, K.; Zhu, L. Q.; Zhang, J. Z.; Shang, L. Y.; Li, Y. W.; Hu, Z. G.; Chu, J. H. Temperature and Pressure Manipulation of Magnetic Ordering and Phonon Dynamics with Phase Transition in Multiferroic $GdFeO_3$: Evidence from Raman Scattering. *Phys. Rev. B* **2020**, *102*, 024103.
(43) Liu, C.; Zhao, G. D.; Hu, T.; Bellaiche, L.; Ren, W. Structural and Magnetic Properties of Two-dimensional Layered $BiFeO_3$ from First Principles. *Phys. Rev. B* **2021**, *103*, L081403.
(44) Bushiri, M. J.; Nayar, V. U. STRUCTURAL ASPECTS OF $KMg_{1/3}Nb_{2/3}PO_5$ (KMNP), A Ktp Analogue-Raman And FTIR Spectroscopic Study. *J. Nonlinear. Opt. Phys.* **2001**, *10*, 345−353.
(45) Sang, S. J.; Yuan, Z. Y.; Zheng, L. M.; Sun, E. W.; Qi, X. D.; Zhang, R.; Jiang, X. N.; Li, S. Y.; Du, J. Raman Spectra of (K,Na)(Nb,Ta)O_3 Single Crystal. *J. Alloys Compd.* **2017**, *704*, 804−808.
(46) Kakimoto, K.; Akao, K.; Guo, Y. P.; Ohsato, H. S. Raman Scattering Study of Piezoelectric $(Na_{0.5}K_{0.5})NbO_3$-$LiNbO_3$ Ceramics. *Jpn. J. Appl. Phys.* **2005**, *44*, 7064−7067.
(47) Zheng, Q. F.; Li, Q.; Xue, S. D.; Wu, Y. H.; Wang, L. J.; Zhang, Q.; Qin, X. M.; Zhao, X. Y.; Wang, F. F.; Yang, W. G. Pressure Driven Structural Evolutions of 0.935$(Na_{0.5}Bi_{0.5})TiO_3$-0.065$BaTiO_3$ Lead-Free Ferroelectric Single Crystal through Raman Spectroscopy. *Chin. Phys. Lett.* **2021**, *38*, 026102.
(48) De la Flor, G.; Malcherek, T.; Gorfman, S.; Mihailova, B. Structural Transformations in (1-x)$Na_{0.5}Bi_{0.5}TiO_3$-x$BaTiO_3$ Single Crystals Studied by Raman Spectroscopy. *Phys. Rev. B* **2017**, *96*, 214102.
(49) Rouquette, J.; Haines, J.; Bornand, V.; Pintard, M.; Papet, P.; Astier, R.; Leger, J. M.; Gorelli, F. Transition to a Cubic Phase with Symmetry-breaking Disorder in $PbZr_{0.52}Ti_{0.48}O_3$ at High Pressure. *Phys. Rev. B* **2002**, *65*, 214102.
(50) Hill, N. A.; Rabe, K. M. First-principles Investigation of Ferromagnetism and Ferroelectricity in Bismuth Manganite. *Phys. Rev. B* **1999**, *59*, 8759.
(51) Tohei, T.; Kuwabara, A.; Yamamoto, T.; Oba, F.; Tanaka, I. General Rule for Displacive Phase Transitions in Perovskite Compounds Revisited by First Principles Calculations. *Phys. Rev. Lett.* **2005**, *94*, 035502.
(52) Smith, K. A.; Ramkumar, S. P.; Harms, N. C.; Clune, A. J.; Xu, X.; Cheong, S.-W.; Liu, Z.; Nowadnick, E. A.; Musfeldt, J. L. Revealing Pressure-driven Structural Transitions in the Hybrid Improper Ferroelectric $Sr_3Sn_2O_7$. *Phys. Rev. B* **2021**, *104*, 064106.
(53) Li, Q. Q.; Wang, J. Y.; Li, M. J.; Guo, S.; Zhang, J. Z.; Hu, Z. G.; Zhou, Z. Y.; Wang, G. S.; Dong, X. L.; Chu, J. H. Structure Evolution Mechanism of $Na_{0.5}Bi_{2.5}Nb_{2-x}W_xO_{9+\delta}$ Ferroelectric Ceramics: Temperature-dependent Optical Evidence and First-principles Calculations. *Phys. Rev. B* **2017**, *96*, 024101.
(54) Glazer, A. M. The Classification of Tilted Octahedra in Perovskites. *Acta Crystallogr. Sect. B* **1972**, *28*, 3384−3392.
(55) Buixaderas, E.; Nuzhnyy, D.; Gregora, I.; Kamba, S.; Berta, M.; Malic, B.; Kosec, M. Lattice Dynamics and Phase Transitions in $KNbO_3$ and $K_{0.5}Na_{0.5}NbO_3$ Ceramics. *IEEE Trans. Ultrason. Ferroelectr. Freq. Control* **2009**, *56*, 1843−1849.
(56) Gupta, H. C.; Archana; Luthra, V. Lattice Vibrations of $ABi_2Nb_2O_9$ Crystals (A = Ca,Sr,Ba). *Vib. Spectrosc.* **2011**, *56*, 235−240.
(57) Srimathy, B.; Jayavel, R.; Ganesamoorthy, S.; Bhaumik, I.; Karnal, A. K.; Natarajan, V.; Varadarajan, E.; Kumar, J. Crystal Growth of PZN-PT Single Crystals and Critical Issues for Higher Piezoelectric Coefficient. *Cryst. Res. Technol.* **2012**, *47*, 523−529.
(58) Zhao, X. Y.; Wang, J. J.; Chen, L. Q. A Thermodynamic Study of Phase Transitions and Electrocaloric Properties of $K_{0.5}Na_{0.5}NbO_3$ Single Crystals. *Appl. Phys. Lett.* **2020**, *116*, 092902.
(59) Chen, K.; Xu, G. S.; Yang, D. F.; Wang, X. F.; Li, J. B. Dielectric and Piezoelectric Properties of Lead-free 0.95$(K_{0.5}Na_{0.5})NbO_3$ C0.05$LiNbO_3$ Crystals Grown by the Bridgman Method. *J. Appl. Phys.* **2007**, *101*, 044103.

https://doi.org/10.1021/acsami.2c13669
ACS Appl. Mater. Interfaces 2022, 14, 45590−45599

(60) Wang, Y. C.; Lv, J.; Zhu, L.; Ma, Y. M. CALYPSO: A Method for Crystal Structure Prediction. *Comput. Phys. Commun.* **2012**, *183*, 2063−2070.
(61) Zhu, L.; Liu, H. Y.; Pickard, C. J.; Zou, G. T.; Ma, Y. M. Reactions of Xenon with Iron and Nickel are Predicted in the Earth's inner Core. *Nat. Chem.* **2014**, *6*, 644−648.
(62) Gao, P. Y.; Tong, Q. C.; Lv, J.; Wang, Y. C.; Ma, Y. M. X-ray Diffraction Data-assisted Structure Searches. *Comput. Phys. Commun.* **2017**, *213*, 40−45.
(63) Pei, S. H.; Wang, Z. H.; Xia, J. High Pressure Studies of 2D Materials and Heterostructures: A Review. *Mater. Design.* **2022**, *213*, 110363.
(64) Mao, H. K.; Xu, J.; Bell, P. M. Calibration of the Ruby Pressure Gauge to 800 kbar Under Quasi-Hydrostatic Conditions. *J. Geophys. Res.* **1986**, *91*, 4673−4676.

https://doi.org/10.1021/acsami.2c13669
ACS Appl. Mater. Interfaces 2022, 14, 45590−45599